Journal of Power Sources 201 (2012) 368–375

Contents lists available at SciVerse ScienceDirect

Journal of Power Sources

journal homepage: www.elsevier.com/locate/jpowsour

High power supercapacitor electrodes based on flexible TiC-CDC nano-felts

Yu Gao[a,b], Volker Presser[b], Lifeng Zhang[c], Jun J. Niu[b], John K. McDonough[b], Carlos R. Pérez[b], Haibo Lin[a], Hao Fong[c,*], Yury Gogotsi[b,**]

[a] College of Chemistry, Jilin University, Changchun 130012, PR China
[b] Department of Materials Science and Engineering, A. J. Drexel Nanotechnology Institute, Drexel University, Philadelphia, PA 19104, USA
[c] Department of Chemistry, South Dakota School of Mines and Technology, Rapid City, SD 57701, USA

ARTICLE INFO

Article history:
Received 6 October 2011
Received in revised form 29 October 2011
Accepted 31 October 2011
Available online 6 November 2011

Keywords:
Carbide-derived carbon
Electrospinning
Nano-felt
Supercapacitor
Titanium carbide

ABSTRACT

Flexible electrospun titanium carbide (TiC) nano-felts were converted into carbide-derived carbon (CDC) by dry chlorination at temperatures between 200 and 1000 °C and used as binder-free supercapacitor electrodes. In the carbide nano-felt, TiC nano-crystals (20–30 nm) were embedded in a matrix of disordered carbon. After chlorination, the porous CDC nano-fibers/felts maintain their size, shape, and flexibility. With the increase of synthesis/chlorination temperature, the degree of carbon ordering increased. Electrochemical characterizations in 1 M H_2SO_4 and 1.5 M tetraethylammonium tetrafluoroborate in acetonitrile were carried out on binder-free electrodes with galvanostatic cycling, cyclic voltammetry, and electrochemical impedance spectroscopy. The highest gravimetric capacitance was identified for the CDC nano-felt synthesized at the highest temperature of 1000 °C, reaching 135 F g^{-1} in aqueous and 120 F g^{-1} in organic electrolytes. In contrast to powder or monolithic supercapacitor electrodes made of conventional activated, templated, or carbide-derived carbons, this material demonstrated excellent high-power handling ability; and ~50% of the low-rate capacitance was maintained at a very high scan rate of 5 V s^{-1}.

1. Introduction

Electrodes used in electrochemical double layer capacitors (EDLC; also known as supercapacitors) are commonly based on a mixture of activated carbon (~85–90 wt.%) with polymeric binder (~5–10 wt.%) and conductive additives (mostly carbon black; ~5 wt.%) [1,2]. While the choice of activated carbons is motivated by high specific surface area and electrical conductivity, the polymeric binder is a processing-related necessity, ensuring mechanical integrity while significantly lowering the conductivity and rate handling ability of the electrodes. The latter is only partially compensated by the addition of carbon black particles which makes another processing step necessary and increases the cost of the device without contributing to capacitance [3]. When compared to activated carbons, carbide-derived carbons (CDC) with their tunable porosity and conductivity have been shown to possess a higher gravimetric and volumetric capacitance [4].

CDCs have been derived from a large number of crystalline (micro- and/or nano-sized) binary and ternary carbides (e.g., SiC, TiC, Ti_2AlC) [4] and polymer-derived carbides (PDC), such as Si–C [5], Si–C–N [6], Si–O–C [7], and Ti–C [8]. PDC–CDCs offer a high level of control over the pore size and surface area. With the presence of micro- and meso-pores, many of them have networks of hierarchical pores which are known to facilitate ion transport required for achieving high power [9–11]. While small pores account for large surface area and, hence, high specific capacitance; larger pores facilitate ion mobility throughout CDC particles. The conformal character of the CDC synthesis ensures that complex shapes and geometries of the PDC are maintained and, thus, can be utilized for advanced device engineering, e.g., manufacturing 3-dimensional textures or conformal energy storage devices.

Supercapacitor electrodes with improved electronic conductivity and rate performance can be produced via elimination of polymer binders and development of binder-free porous electrodes showing improved ion accessibility. Binder-free micro-supercapacitors produced by following either the top-down approach (carbide thin films were transformed into carbon and subsequently patterned) [12] or the bottom-up approach (electrophoretic deposition of carbon particles on a patterned current collector [13] or growth of CNT arrays [14]) have demonstrated improved rate handling ability compared to conventional polymer-bonded electrodes. Previous research has indicated that electrospinning can be used to prepare carbon-based electrodes for supercapacitors [15] or lithium-ion batteries [16]. A high power

* Corresponding author. Tel.: +1 605 394 1229; fax: +1 605 394 1232.
** Corresponding author. Tel.: +1 215 895 6446; fax: +1 215 895 1934.
E-mail addresses: hao.fong@sdsmt.edu (H. Fong), gogotsi@drexel.edu (Y. Gogotsi).

0378-7753/$ – see front matter © 2011 Elsevier B.V. All rights reserved.
doi:10.1016/j.jpowsour.2011.10.128

performance has been demonstrated for electrospun carbon fibers [17] and very recently [8], we developed a microporous carbon nano-felt from a pre-ceramic polymeric precursor that maintained mechanical flexibility and showed stable electrochemical performance over tens of thousands of charge-discharge cycles. CDC fiber/felt electrodes derived from a pre-ceramic precursor have three levels of porosity: large inter-fiber pores (ensuring ion accessibility across the entire thickness of the electrode; tens of nanometers), mesopores (facilitating ion transport through the cross-section of individual fibers), and micropores (providing large surface area and, thus, high capacitance). As the inter-particle resistance is eliminated in continuous fiber networks, electron transport is improved and the rate handling ability increases accordingly.

Our previous work [8] illustrated the proof-of-concept of CDC nano-felt electrodes derived from electrospun TiC nano-fiber. In this study, we have systematically investigated parametric correlations among the synthesis conditions (temperature), the CDC nano-felt structures (carbon ordering, pore size, pore size distribution, and surface area), and the resulting properties (conductivity, series resistance, capacitance, and rate handling ability).

2. Materials and methods

2.1. Material synthesis

The TiC nano-fibrous mats (nano-felts) were prepared through following the procedure reported in Ref. [18]. Titanium(IV) *n*-butoxide (TiBO) and furfuryl alcohol (FA) were selected as the titanium and carbon sources, respectively. Polyvinylpyrrolidone (PVP) was used as the carrying polymer for electrospinning, *N*,*N*-dimethylformamide (DMF) was used as the solvent for making a spin dope, and acetic acid (HAc) was added into the spin dope as the catalyst for hydrolysis of TiBO and polymerization of FA. The optimum spin dope contained 10 wt.% TiBO, 10 wt.% FA, 10 wt.% PVP, and 2.5 wt.% HAc. An 18-gauge stainless-steel needle with a 90° blunt tip was adopted as the spinneret, and a positive voltage of 15 kV was applied to the spinneret during electrospinning. A 25 cm diameter roller covered with aluminum foil was used as the nanofiber collector; the roller speed was set at 100 rpm, and the needle-roller distance was set at 25 cm. Four days after electrospinning, the 200 μm thick nanofibrous mat was removed from the aluminum foil, and subsequently pyrolyzed first at 325 °C in air and then at 1400 °C in argon.

TiC nano-felts were placed on a quartz boat and inserted into a horizontal tube furnace (quartz glass), purged in argon flow and heated at 20 °C min^{-1} to the desired temperature (200–1200 °C), and then exposed to the flow of dry chlorine gas (10–15 cm^3 min^{-1}) for 3 h. After chlorination, the nano-felts were annealed at a set temperature (200–600 °C) for 2 h under flowing hydrogen, to remove residual chlorine and chlorides trapped in pores. The hydrogen treatment was carried out either at the synthesis temperature for samples chlorinated at/or below 600 °C, and at 600 °C for samples chlorinated at higher temperatures.

2.2. Structural characterization

Microscopic analyses were carried out via scanning electron microscopy (SEM; Zeiss Supra 50 VP, operating at 5 kV) and transmission electron microscopy (TEM; JEOL, 2010F, operating at 200 kV). TEM specimens were prepared by dispersing the samples in isopropanol followed by placing the suspensions over copper grids with lacey carbon film. SEM samples were mounted on a carbon stub and analyzed without conductive coatings. Raman spectroscopy was carried out with an inVia confocal Raman microspectrometer (Renishaw) using an Ar ion laser (488 nm, ~1 μm lateral spot size) for excitation. A Lorentzian function was assumed for peak fitting and spectral deconvolution. X-ray diffraction (XRD) was carried out using a Siemens D500 diffractometer with Cu-Kα radiation (λ = 1.5406 Å) operating at 30 mA and 40 kV. The XRD patterns were collected using step scans with the step of 2θ being 0.01° and the count time of 2 s per step between the 2θ of 10° and 80°.

2.3. Pore characterization

Prior to gas sorption analysis, all samples were degassed at 200 °C in low vacuum (0.1 Torr) for 24 h to remove the adsorbed species. Gas adsorption analysis using N_2 (at −196 °C) as the adsorbate was conducted with the Quadrasorb surface area and pore size analyzer (Quantachrome Instruments). With the information from N_2 sorption (covering the range of 0.6–50 nm), the pore size distribution (PSD) and specific surface area (SSA) were calculated and the experimental error was approximately 10–15%. Assuming slit-shaped pores, the quenched solid density functional theory (QSDFT) was used [19]. The BET SSA [20] was calculated in the linear regime between 0.05 and 0.30 P/P_0 [21]. With a type IV isotherm and a hysteresis loop, only the adsorption branch was used for calculation of the PSD from N_2 sorption. The average pore size was calculated as the volume-weighted average pore diameter.

2.4. Electrochemical characterization

Symmetrical two-electrode cells were assembled with stainless-steel (aqueous electrolyte) or aluminum (organic electrolyte) current collectors and Gore PTFE separator. The current collectors were coated with a carbon-based conductive paint to minimize the contact resistance with the electrode. Electrochemical characterization in 1 M H_2SO_4 (10 × 5 mm^2 cell) and 1.5 M TEA-BF_4 (10 × 10 mm^2 cell) in acetonitrile was carried out using galvanostatic cycling, cyclic voltammetry, and impedance spectroscopy. Nano-felts were used as produced without the addition of any polymeric binder and/or conductive additive and directly placed on the current collector. Time constants and frequency dispersion were analyzed via impedance spectroscopy. Cyclic voltammetry was performed at scanning rates between 0.01 V s^{-1} and 100 V s^{-1} within a voltage window of −0.5 to 0.6 V. Specific capacitance '*C*' was calculated from galvanostatic cycling using Eq. (1):

$$C = \frac{2i}{m(dV/dt)} \quad (1)$$

where m is the carbon mass of one electrode, i is the discharge current and dV/dt is the slope of the discharge curve.

From cyclic voltammetry, the capacitance can be derived through the Eq. (2):

$$C = \frac{2(1/\Delta E)\int i dV/v}{m} \quad (2)$$

where ΔE is the voltage window, i is the discharge current, V is the voltage, and v is the scan rate.

The EDLCs were tested at constant current charge/discharge regimes (between 10 and 100 mA cm^{-2}) within the voltage range from −0.5 to 0.6 V in 1 M H_2SO_4. The impedance complex plane (Z', $-Z''$) plots (Nyquist plots) for EDLCs have been measured within the range of AC frequency f from 10^{-2} to 10^5 Hz and at fixed cell voltage of 0 V (Z' is the real part and Z'' is the imaginary part of the impedance, respectively).

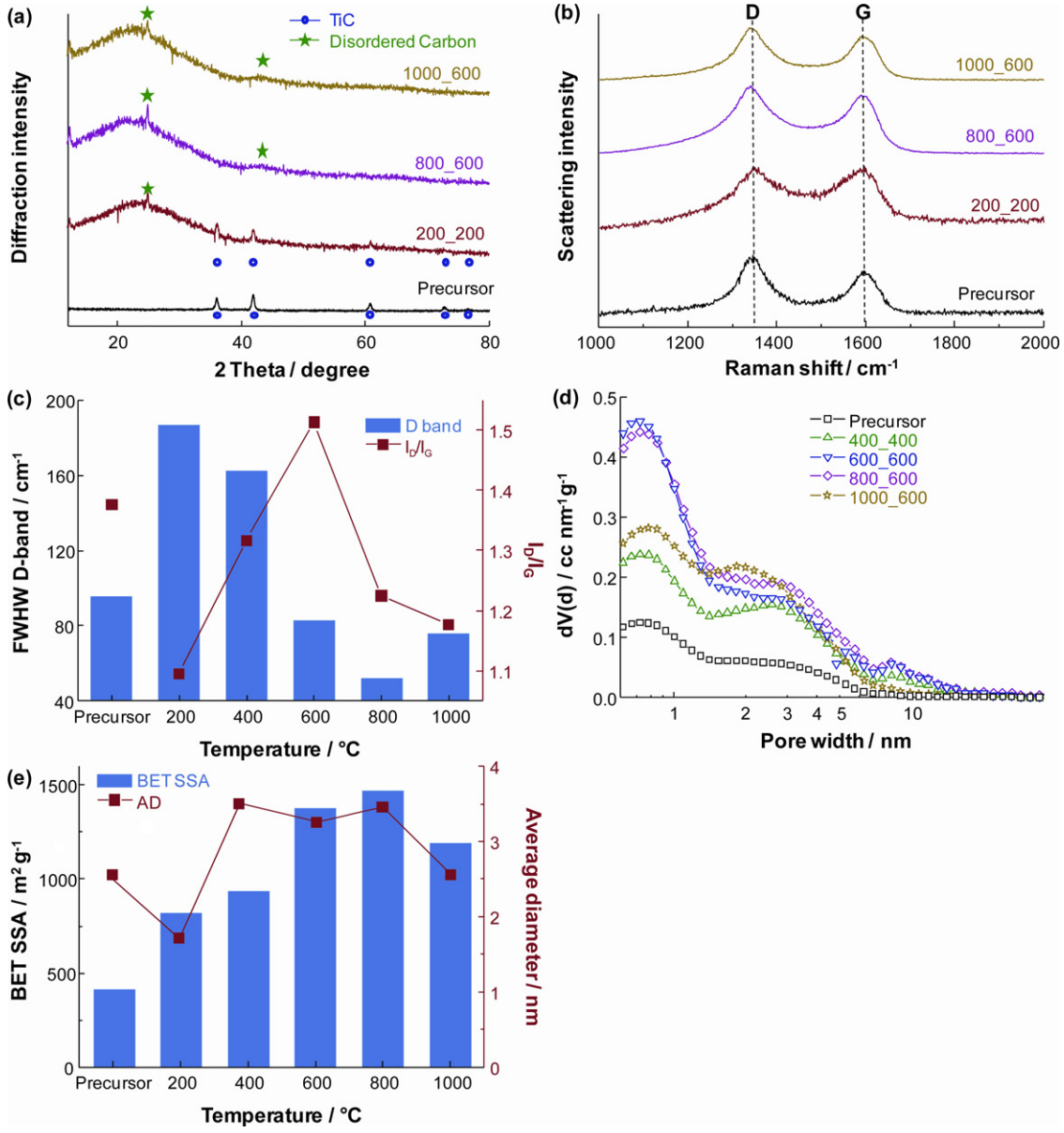

Fig. 1. XRD pattern (a) and Raman spectra (b) of TiC-CDC nano-felts and their precursor of electrospun TiC nano-fibrous felt. The dependence of FWHW of D-band and ID/IG ration on the synthesis temperature (c). Pore size distributions (d). SSA and average pore diameter as a function of chlorination temperature (e).

3. Results and discussion

3.1. Structure of TiC-CDC nano-felts

XRD was carried out to investigate the structural changes in the TiC-CDC nano-felts under different chlorination conditions. Fig. 1a shows that chlorination selectively extracts Ti from the electrospun TiC nano-fibers/felts, with trace amounts of un-reacted nano-TiC (<5 wt.%) found only in the TiC-CDC nano-felt sample chlorinated at 200 °C. The two very broad peaks centered at the 2θ angles of ~24° and ~44° were attributed to diffuse scattering from disordered carbon. The absence of sharp peaks corresponding to graphite indicates the disordered nature of TiC-CDC.

Raman spectra of the electrospun TiC precursor and TiC-CDC nano-felts are shown in Fig. 1b. The spectra show the two characteristic peaks for carbon: (i) the D-mode at 1342–1353 cm^{-1} that is characteristic for disordered carbon with finite sizes of crystallites, and (ii) the graphite G-mode at 1590–1601 cm^{-1} (Fig. 1b). In the spectra from the TiC precursor, only Raman peaks of carbon can be seen related to the D- and G-modes [22,23] of graphitic and disordered carbon present in the precursor fibers. All Raman modes of TiC-CDC nano-felt prepared by chlorination at 200 °C have a larger full-width at half maximum (FWHW) compared to the precursor and the FWHM further decreases with the increase of the chlorination temperature (Fig. 1c). Before chlorination, the carbon related signal corresponds to 25–30 wt% of amorphous carbon surrounding the nanocrystalline TiC grains. This carbon phase is more ordered (i.e., it shows more narrow Raman modes) than the carbon derived from low temperature chlorination of TiC. After chlorination, the initially present carbon phase still contributes to the Raman signal; the latter, however, is dominated by the signal from the TiC-CDC which shows the typical dependency of CDC for of the carbon ordering on the chlorination temperature, and the fraction of graphitic carbon increases with temperature [4].

Nitrogen sorption was used to characterize the PSD, the SSA, and the pore volume of TiC-CDC nano-felts and the precursor (Fig. 1d and e, and Table 1). Table 1 shows that raising the chlorination temperature increases the SSA and volume of pores. The precursor has a

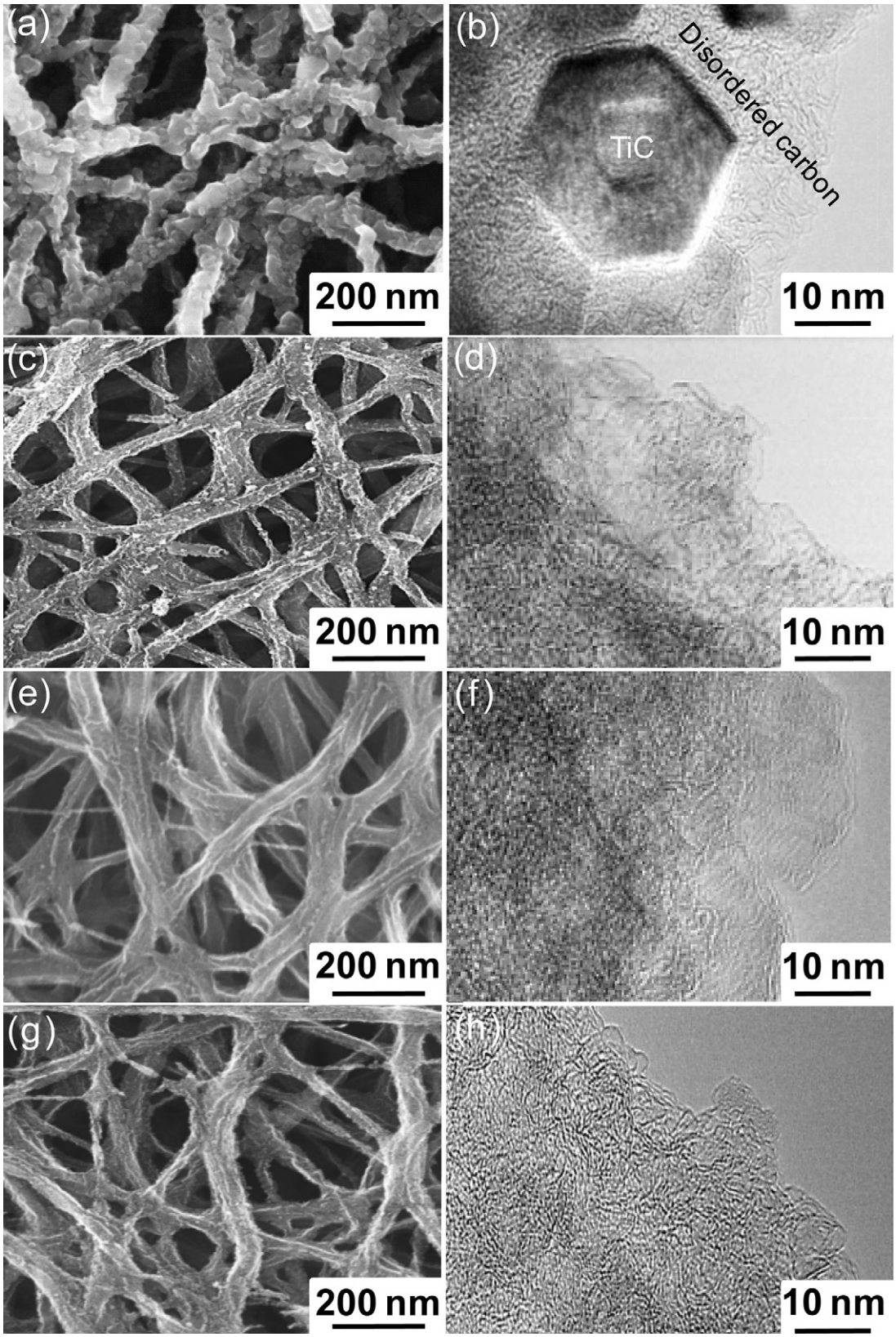

Fig. 2. SEM (a, c, e, and g) and TEM (b, d, f, and h) images of the as-received TiC-CDC nano-felts (a and b) and samples after chlorination at 200 (c and d), 800 (e and f), and 1000 °C (g and h).

SSA value of 384 $m^2\ g^{-1}$, an average pore size of 2.55 nm, and a pore volume of 0.33 $cm^3\ g^{-1}$. The BET SSA increases from 935 $m^2\ g^{-1}$ at 400 °C to 1468 $m^2\ g^{-1}$ at 800 °C and the total pore volume increases from 0.98 to 1.43 $cm^3\ g^{-1}$, respectively (Fig. 1e). After chlorination at 800 °C, the average pore size is 3.46 nm (Table 1) with the more narrow PSD of the studied samples, while the smallest average pore size has been found after chlorination at 200 °C (1.75 nm). The combination of nano-scale pores, partially graphitic carbon (which is

Table 1
Values of SSA, pore size, and pore volume acquired from N_2 gas sorption for TiC-CDC nano-felts and the precursor at −196 °C.

	BET SSA[a] ($m^2\ g^{-1}$)	DFT SSA[b] ($m^2\ g^{-1}$)	Total pore volume ($cm^3\ g^{-1}$)	Average pore size[c] (nm)
Precursor	409	384	0.33	2.55
Nano-felt (200 °C)	862	795	0.56	1.75
Nano-felt (400 °C)	935	843	0.98	3.55
Nano-felt (600 °C)	1374	1430	1.27	3.25
Nano-felt (800 °C)	1468	1352	1.43	3.46
Nano-felt (1000 °C)	1188	834	0.95	2.56

[a] The BET SSA [20] was calculated in the linear regime between 0.05 and 0.30 P/P_0 [21].
[b] DFT SSA was calculated assuming slit-pore geometry using QSDFT deconvolution [19].
[c] The average pore size is the volume-weighted average diameter based on QSDFT data.

electrically conductive), and continuous fibers makes the TiC-CDC nano-felts attractive for the application of supercapacitor electrode.

As seen from electron micrographs (Fig. 2), the TiC precursor is composed of TiC nanocrystals embedded in a carbon matrix with 1–3 layers of graphitic carbon surrounding the TiC crystals (Fig. 2b). SEM and TEM images (Fig. 2) show a gradual structural evolution with increasing chlorination temperature. At 200 °C (Fig. 2d), the TiC-CDC nano-felts consist predominantly of amorphous carbon with the graphitic contributions being only the residual graphite layers around former TiC nanocrystals that have been completely transformed into CDC (Fig. 2c and d). Higher chlorination temperatures correspond to higher carbon mobility (Fig. 2e–h), which is consistent with Raman and XRD analyses. At the highest synthesis temperature (1000 °C), the fibers in the TiC-CDC nano-felt consist of a pore network in which pores are separated by one or two carbon layers only.

3.2. Electrochemical measurements

Cyclic voltammograms (CVs) of the nano-felt precursor and the TiC-CDC nano-felts at 0.01 V s^{-1} scan rate in 1 M H_2SO_4 (Fig. 3a) show that the capacitance increases with the chlorination temperature. Minor electrochemical reactions occur as evidenced by small peaks in the CVs for the 800 °C and 1000 °C samples as related to surface functional groups. Contrary to the observations for microparticulate TiC-CDC powder [24], the rectangular shape of the CV curves indicates more purely capacitive behavior meaning that at this scan rate, the equivalent series resistance (ESR) of the electrode related to the hindrance of ion motion in the pores is low. In aqueous electrolyte, a maximum capacitance of 135 F g^{-1} from cyclic voltammetry was obtained from the felt synthesized at the highest chlorination temperature (Fig. 3b and Table 2) which is in agreement with galvanostatic charge/discharge measurements

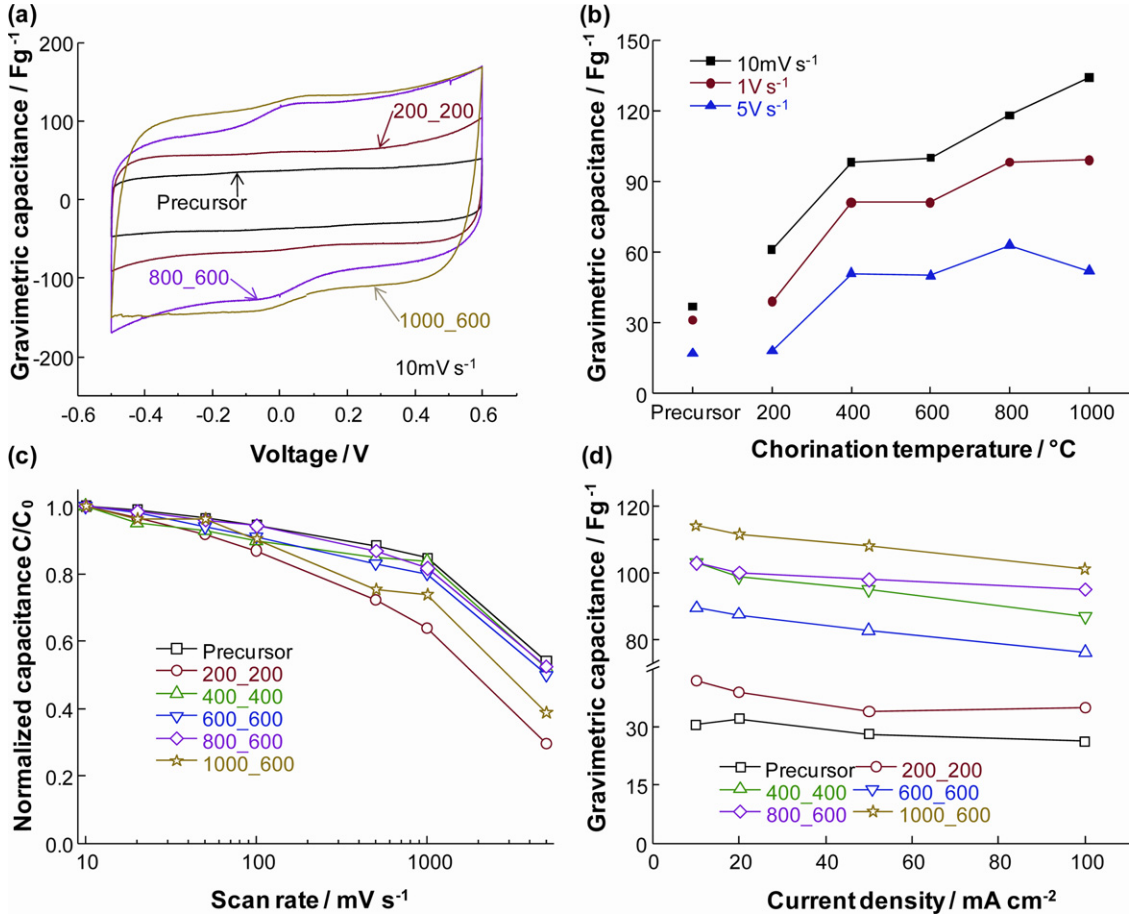

Fig. 3. Cyclic voltammograms of the TiC-CDC nano-felts at 0.01 V s^{-1} (a) and the gravimetric capacitance of TiC-CDC nano-felts and precursor at different scan rate in 1 M H_2SO_4 (b). The power-handling ability of TiC-CDC nano-felts and precursor were revealed when plotting the scan rate vs. the normalized capacitance C/C_0 (c). Gravimetric capacitance obtained via galvanostatic charge/discharge measurements for the TiC-CDC nano-felts and precursor (d).

Table 2
Electrochemical results for TiC-CDC nano-felts and the precursor (CV, cyclic voltammetry; GC, galvanostatic charge/discharge) tested in 1 M H_2SO_4.

	Gravimetric capacitance ($F g^{-1}$)		Time constant (s)	Resistance (Ω cm^2)
	CV	GC		
Precursor	37	30	0.455	1.1
Nano-felt (200 °C)	65	42	0.420	1.7
Nano-felt (400 °C)	94	90	0.337	1.5
Nano-felt (600 °C)	107	103	0.322	1.2
Nano-felt (800 °C)	118	103	0.303	1.2
Nano-felt (1000 °C)	135	120	0.088	1.0

($120 F g^{-1}$); the TiC-CDC nano-felt chlorinated at 1000 °C has a high, but not the highest, SSA but the smallest average pore diameter compared to other nano-felts.

All samples showed a high rate handling ability, as seen from Fig. 3c. The best performance at high charge/discharge rates was seen for either TiC-CDC synthesized at high temperatures (≥600 °C) or the TiC nano-felt precursor, with TiC precursor having an overall small gravimetric capacitance ($37 F g^{-1}$). At a sweep rate of $0.01 V s^{-1}$, the TiC-CDC nano-felt made from chlorination at 1000 °C yielded the highest capacitance of $135 F g^{-1}$ that dropped to 74% of the initial value at $\sim 1 V s^{-1}$ and to 40% with high rate of $5 V s^{-1}$ (Fig. 3c and Table 2). The TiC-CDC nano-felts (400, 600, and 800 °C) maintained more than 80% of the initial value at $\sim 1 V s^{-1}$ and 50% at $5 V s^{-1}$. The loss of capacitance is caused by an increase of the ion transport related resistance and causes conventional activated carbon or carbide-derived carbon powder electrodes to lose their capacitance quickly at scan rates above $0.1 V s^{-1}$; thus, their maximum charge/discharge rates are substantially limited. Bleda-Martinez et al. reported the decrease of capacitance to below 5% of the initial value at the sweep rate of $0.1 V s^{-1}$ for activated carbon fibers (ACF) in 1 M Na_2SO_4 [25]. At this scan rate, except for the felt made from chlorination at 200 °C (maintained 86%), other nano-felts maintained more than 90% capacitance of the initial value.

The time constant and resistance of the TiC-CDC nano-felts and the precursor are plotted in Fig. 4a and Table 2. It is apparent that the time constant and resistance for 1000 °C felt is lower compared to other felts. It is considered that the advantageous microstructure of TiC-CDC nano-felts, such as a 3-D network, the presence of hierarchic mesopores, and the amorphous free carbon, would jointly contribute to the high power performance. In addition, the fiber structure minimizes the electrolyte diffusion distance to the interior surface area.

To study the effect of frequency on the carbon electrodes, EIS was performed. Nyquist plots for TiC-CDC nano-felts and precursor (Fig. 4b and Table 2) show a moderate equivalent series resistance, calculated as the intercept that the linear region makes with the real impedance axis, for all samples. Also evident from Fig. 4b is the semi-circle that occurs at moderate frequencies which is attributed to the interface between the carbon film and current collector interfacial resistance. In the low frequency regime, capacitors assembled from CDCs synthesized at all temperatures show ideal capacitive behavior, with a near vertical line parallel to the imaginary axis.

Fig. 4c shows the evolution of real capacitance C' versus frequency and Fig. 4d shows the evolution of the imaginary capacitance C'' with frequency from which the time constant τ can be derived. For most nano-felts, there is little change in the time constant. The corresponding time constant of most TiC-CDC nano-felts was around 0.350 s (except for the felt synthesized at 1000 °C, which was 0.088 s) compared to 200 s for conventional TiC-CDC synthesized at 600 °C [26], 0.700 s for MWCNT [27], and 0.026 s for carbon-onion micro-supercapacitors [17]. As expected, both series

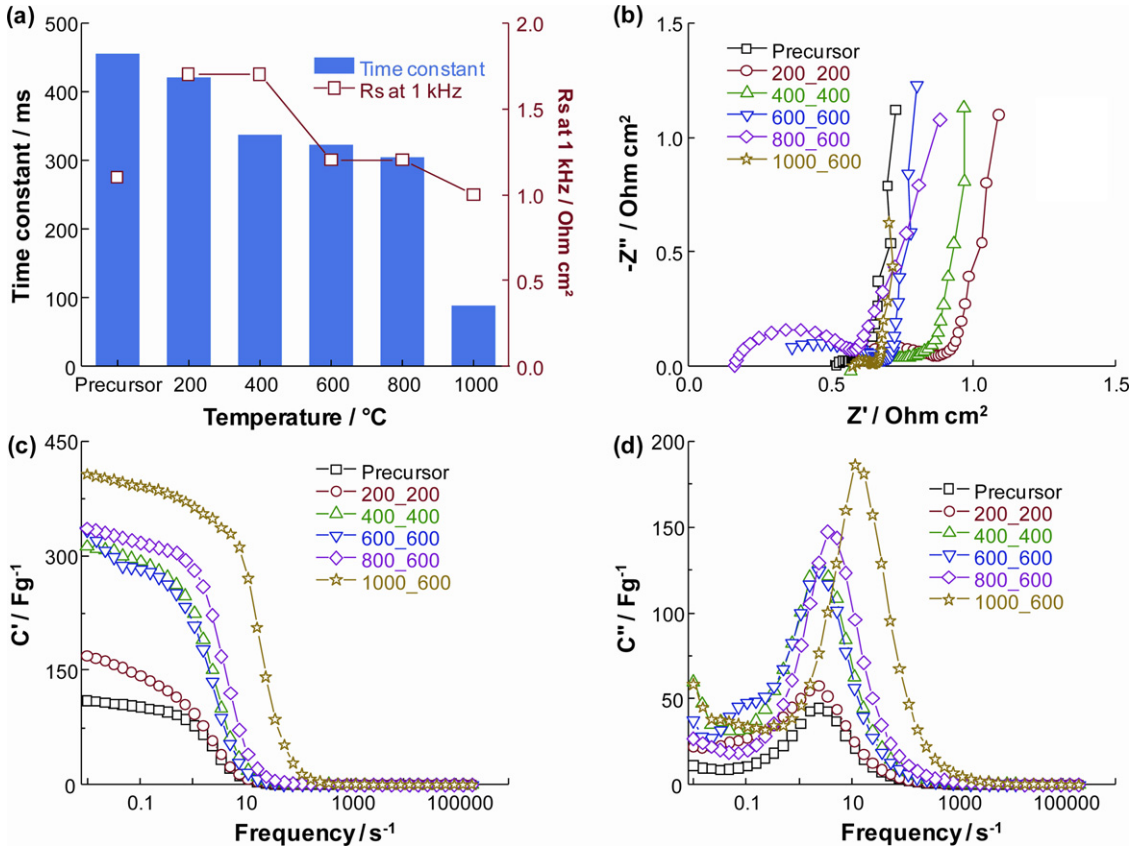

Fig. 4. The time constant and resistance in 1 M H_2SO_4 in comparison with the precursor (a). Nyquist plots for TiC-CDC nano-felts and precursor (b). Progression of the real capacitance, C', for TiC-CDC nano-felts and precursor with frequency (c), and the imaginary capacitance, C'', for TiC-CDC nano-felts and precursor as a function of frequency (d).

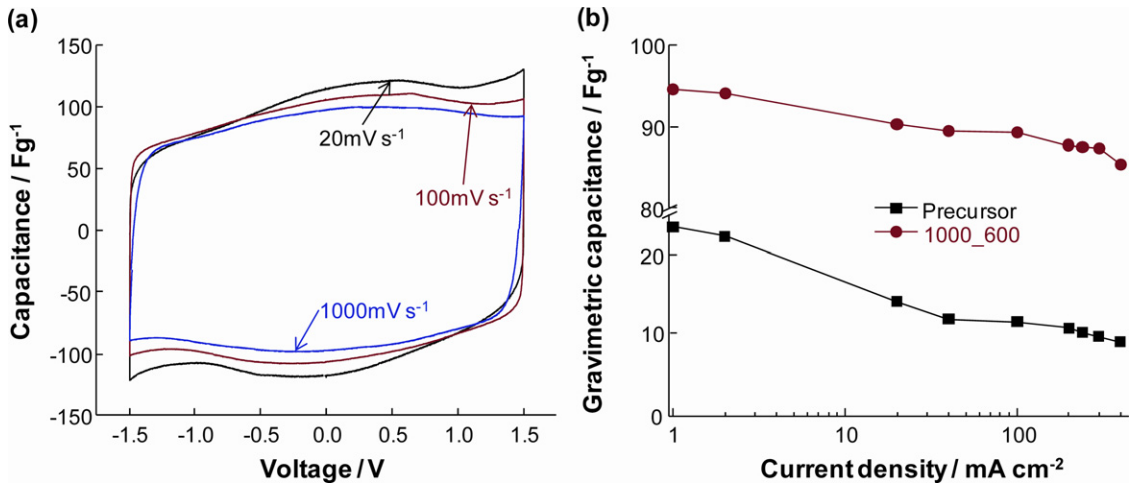

Fig. 5. Cyclic voltammograms of 1000 °C TiC-CDC nano-felt in 1.5 M TEA-BF_4 (a). Gravimetric capacitance obtained via galvanostatic charge/discharge measurements for 1000 °C TiC-CDC nano-felt and the precursor in organic electrolyte (b).

Table 3
Electrochemical results for TiC-CDC nano-felt synthesized at 1000 °C and the precursor (CV, cyclic voltammetry; GC, galvanostatic charge/discharge) tested in 1.5 M TEA-BF_4.

	Gravimetric capacitance ($F g^{-1}$)		Time constant (s)	Resistance (Ωcm^2)
	CV	GC		
Precursor	30	24	0.417	2.7
Nano-felt (1000 °C)	120	95	0.284	1.4

resistance and time constants decrease with increased synthesis temperatures, due to increased order in the resulting carbon. The presence of pre-existing amorphous carbon structures in the precursor fibers explains (Fig. 2) its relatively high conductivity.

The TiC-CDC nano-felts (1000 °C) were also tested in 1.5 M TEA-BF_4 with galvanostatic charge/discharge and cyclic voltammetry (Fig. 5 and Table 3). At a slow scan rate of 0.01 V s^{-1}, a gravimetric capacitance of 120 F g^{-1} was measured in organic electrolytes (Fig. 5a and Table 3). The 1000 °C TiC-CDC nano-felts showed an extremely high rate handling ability in organic electrolytes, as seen from Fig. 5b enabling the use of TiC-CDC nano-felt electrodes above 1 V s^{-1}. At a sweep rate of 0.01 V s^{-1}, the 1000 °C TiC-CDC nano-felt yielded the high capacitance of 95 F g^{-1} that dropped by only 5% at 1 V s^{-1} (Fig. 5b and Table 3). Table 3 shows that the time constant and resistance for 1000 °C TiC-CDC nano-felt (0.284 s, 1.4 Ωcm^2) are much lower than for the precursor (0.417 s, 2.7 Ωcm^2) in organic electrolytes. Even for the highest capacitance (1000 °C TiC-CDC nano-felt in aqueous electrolyte: 135 F g^{-1}), the volumetric capacitance is fairly low (19 F cm^{-3}) because of the low nano-felt density (0.14 g cm^{-3}). While this value indeed is small compared to monolithic TiC-CDC films (>100 F cm^{-3}) [28], it is still higher compared to onion-like carbon micro-supercapacitors (~10 F cm^{-3}) [29]. We note, however, that the high volumetric capacitance of monolithic CDC films is only achieved for very thin films and both, capacitance and rate handling ability drop with increasing the film thickness to beyond 50 μm (for comparison: the nano-felt thickness was 200 μm).

4. Conclusion

In summary, the TiC-CDC nano-felts with superior electrochemical properties were developed through chlorination of electrospun TiC nano-fibrous felts. The TiC-CDC nano-felts retained the morphological properties of the precursor, while having substantially higher values of SSA and pore volume. Low synthesis temperature (below 400 °C) resulted in a narrow PSD and amorphous structure. Increasing the synthesis temperature to 600 °C and above resulted in a more ordered carbon structure with much more micropores and a broader PSD. The developed TiC-CDC nano-felts demonstrated excellent high-power performance when used as an electrode material for electrochemical capacitors.

The electrochemical characterization showed that the nano-felts still retained more than 90% of their low rate capacitance at a scan rate of 0.1 V s^{-1} in aqueous electrolyte and the nano-felts synthesized at temperature between 400 and 800 °C lost less than 50% of capacitance at scan rates as high as 5 V s^{-1}. The 1000 °C nano-felt dropped just 5% at ~1 V s^{-1} in organic electrolyte, which is a less significant decrease in capacitance as compared to the activated carbon or conventional TiC-CDC powder or bulk electrodes, which are considered to be the best materials for supercapacitor electrodes. The highest capacitance was 135 F g^{-1} in aqueous and 120 F g^{-1} in organic electrolyte (synthesized at 1000 °C). The rates above 1 V s^{-1} have only been achieved for nanotubes, carbon onions, and graphene, but those have a lower capacitance when compared to the TiC-CDC nano-felts. This is due to the microstructure of the TiC-CDC nano-felts; i.e., the disordered and extremely porous carbon coexisting with graphitic carbon ribbons in the nanofiber network. The structural integrity and resilience of the developed TiC-CDC nano-felts would make them suitable for energy-related applications, particularly as binder-free and flexible supercapacitor electrodes.

Acknowledgements

Yu Gao acknowledges financial support by the China Scholarship Council. Volker Presser acknowledges financial support by the Alexander von Humboldt Foundation. Hao Fong acknowledges financial support by the U.S. Department of Energy (award number: DE-FG02-08ER64624). Raman spectroscopy was carried out on instrumentation of the W.M. Keck Institute for Attofluidic Nanotube-Based Probes. The authors acknowledge the use of XRD, TEM, and SEM in the Centralized Research Facilities (CRF) of Drexel University. Kristy Jost (Drexel University) is thanked for helpful discussions.

References

[1] E. Frackowiak, F. Béguin, Carbon 39 (2001) 937–950.
[2] A. Burke, Journal of Power Sources 91 (2000) 37–50.

[3] J.R. Miller, A.F. Burke, The Electrochemical Society Interface 17 (2010) 53–57.
[4] V. Presser, M. Heon, Y. Gogotsi, Advanced Functional Materials 21 (2011) 810–833.
[5] Y. Korenblit, M. Rose, E. Kockrick, L. Borchardt, A. Kvit, S. Kaskel, G. Yushin, ACS Nano 4 (2010) 1337–1344.
[6] S.-H. Yeon, P. Reddington, Y. Gogotsi, J.E. Fischer, C. Vakifahmetoglu, P. Colombo, Carbon 48 (2010) 201–210.
[7] C. Vakifahmetoglu, V. Presser, S.-H. Yeon, P. Colombo, Y. Gogotsi, Microporous and Mesoporous Materials 144 (2011) 105–112.
[8] V. Presser, L. Zhang, J.J. Niu, J. McDonough, C. Perez, H. Fong, Y. Gogotsi, Advanced Energy Materials 1 (2011) 423–430.
[9] M. Eikerling, A.A. Kornyshev, E. Lust, Journal of the Electrochemical Society 152 (2005) E24–E33.
[10] D.-W. Wang, F. Li, M. Liu, G.Q. Lu, H.-M. Cheng, Angewandte Chemie International Edition 47 (2008) 373–376.
[11] M. Rose, Y. Korenblit, E. Kockrick, L. Borchardt, M. Oschatz, S. Kaskel, G. Yushin, Small 7 (2011) 1108–1117.
[12] M. Heon, S. Lofland, J. Applegate, R. Nolte, E. Cortes, J.D. Hettinger, P.-L. Taberna, P. Simon, P. Huang, M. Brunet, Energy and Environmental Science 4 (2011) 135–138.
[13] D. Pech, M. Brunet, H. Durou, P. Huan, V. Mochalin, Y. Gogotsi, P.-L. Taberna, P. Simon, Nature Nanotechnology 5 (2010) 641–654.
[14] R. Lin, P.-L. Taberna, S. Fantini, V. Presser, C.R. Perez, F. Malbosc, N.L. Rupesinghe, K.B.K. Teo, Y. Gogotsi, P. Simon, The Journal of Physical Chemistry Letters 2 (2011) 2396–2401.
[15] S.A. Kazaryan, S.V. Litvinenko, G.G. Kharisov, Journal of the Electrochemical Society 155 (2008) A464–A473.
[16] M. Hahn, M. Bärtsch, B. Schnyder, R. Kötz, O. Haas, M. Carlen, D. Evard, PSI Scientific Report 2000 V (2001) 67–69.
[17] C. Kim, Applied Physics Letters 83 (2003) 1216.
[18] L. Zhang, J.Y. Howe, Y. Zhang, H. Fong, Crystal Growth & Design 9 (2009) 667–670.
[19] P.I. Ravikovitch, A.V. Neimark, Langmuir 22 (2006) 11171–11179.
[20] S. Brunauer, L.S. Deming, W.E. Deming, E. Teller, Journal of the American Chemical Society 62 (1940) 1723–1732.
[21] Determination of the Specific Surface Area of Solids by Gas Adsorption - BET Method. ISO/DIS 9277, 2008.
[22] A.C. Ferrari, J. Robertson, Physical Review B 61 (2000) 14095–14107.
[23] J. Robertson, Advances in Physics 35 (1986) 317–374.
[24] J. Chmiola, G. Yushin, R.K. Dash, E.N. Hoffman, J.E. Fischer, M.W. Barsoum, Y. Gogotsi, Electrochemical and Solid-State Letters 8 (2005) A357–A360.
[25] M.J. Bleda-Martiĩnez, D. Lozano-Castelloĭ, D. Cazorla-Amoroĩs, E. Moralloĩn, Energy Fuel 24 (2010) 3378–3384.
[26] J. Chmiola, G. Yushin, R. Dash, Y. Gogotsi, Journal of Power Sources 158 (2006) 765–772.
[27] C. Portet, G. Yushin, Y. Gogotsi, Carbon 45 (2007) 2511–2518.
[28] J. Chmiola, C. Largeot, P.L. Taberna, P. Simon, Y. Gogotsi, Science 328 (2010) 480–483.
[29] D. Pech, M. Brunet, H. Durou, P. Huang, V. Mochalin, Y. Gogotsi, P.-L. Taberna, P. Simon, Nature Nanotechnology 5 (2010) 651–654.